scientific reports

Check for updates

OPEN

Precise forecasting of shear stress, viscosity, and density for an aqueous $CuO/CaCO_3/SiO_2$ ternary hybrid nanofluid utilizing the artificial neural network

Yi Jin[1], Ali Basem[2], Ahmed Kateb Jumaah Al-Nussairi[3,10], Muthanna K. Kareem[4], Alimohammadi Hasanabad[5]✉, Zhenghui Li[1] & Soheil Salahshour[6,7,8,9]

The accurate prediction of thermophysical properties in hybrid nanofluids is crucial for enhancing the efficiency of advanced heat transfer and energy conversion systems. Most published research has largely concentrated on single- or binary-nanoparticle systems, and ternary hybrid systems are still poorly understood in terms of interactions. The present study, however, developed two-layer feedforward artificial neural networks to predict shear stress, viscosity, and density for a water-based nanofluid containing copper oxide, calcium carbonate, and silicon dioxide in volume ratios of 60, 30, and 10%, respectively. Training and validation of the networks were based on experimental data collected at temperatures ranging from 25 to 70 °C and nanoparticle volume fractions ranging from 0.5 to 3%. That model achieved outstanding predictive performance, with average root-mean-square errors (evaluated via K-fold cross-validation) of 0.0008 Pa for shear stress, 0.0097 mPa s for viscosity, and 0.0003 g/cm³ for density. Minimum mean squared errors were 1.63×10^{-6}, 3.11×10^{-5}, and 4.03×10^{-5}, respectively, with correlation coefficients over 0.999 across all data sets. The calculated maximum relative errors were 0.71% for shear stress, 1.34% for viscosity, and 0.06% for density, which endorse the reliability and precision of the produced model. Further sensitivity analysis demonstrated that temperature dominance over shear stress and viscosity, although nanoparticle concentration exerted a significantly stronger impact on density. The proposed framework served as an accurate, data-driven tool for modeling ternary hybrid nanofluids, providing practical insights into their optimized formulations for high-performance thermal management applications.

Keywords Artificial neural network, Viscosity, Shear stress, Density, Hybrid nanofluid, $CuO/CaCO_3/SiO_2$

Abbreviations

ANN	Artificial neural network
μ_{nf}	Viscosity
D	Density
MSE	Mean squared error
R	Correlation coefficients
$CaCO_3$	Calcium carbonate
HF	Heat transfer
TC	Thermal conductivity

[1]College of Chemical and Material Engineering, Quzhou University, Quzhou 324000, Zhejiang, People's Republic of China. [2]Faculty of Engineering, Warith Al-Anbiyaa University, Karbala 56001, Iraq. [3]Al-Manara College for Medical Sciences, Amarah, Maysan, Iraq. [4]Department of Mechanical Engineering, University of New Hampshire, Durham, NH 03824, USA. [5]Fast Computing Center, Shabihsazan Ati Pars, Tehran, Iran. [6]Faculty of Engineering and Natural Sciences, Istanbul Okan University, Istanbul, Turkey. [7]Faculty of Engineering and Natural Sciences, Bahcesehir University, Istanbul, Turkey. [8]Research Center of Applied Mathematics, Khazar University, Baku, Azerbaijan. [9]Faculty of Science and Letters, Piri Reis University, Tuzla, Istanbul, Turkey. [10] Mathematics Department, College of Basic Education, University of Misan, Misan 62001, Iraq. ✉email: alimohammadihasanabad@outlook.com

SiO_2	Silicon dioxide
τ	Shear stress
HNFs	Hybrid nanofluids
NPs	Nanoparticles
ϕ	Volume fraction
H_2O	Water
T	Temperature

Nanofluids (NFs), defined as suspensions of nanoparticles (NPs) in base fluids, have garnered significant interest over the past few decades due to their enhanced thermophysical and heat transfer (HT) properties[1,2]. The NPs significantly improve thermal conductivity (TC), viscosity (μ_{nf}), specific heat capacity, and convective HT, making NFs one of the most promising materials for advanced thermal management in energy systems, electronic cooling, and industrial processes[3,4]. Among the most commonly used NPs, SiO_2, $CaCO_3$, and CuO are distinct because of certain advantages: SiO_2 has excellent thermal and hydrodynamic stability; $CaCO_3$ has biocompatibility and is inexpensive; CuO is an enhancement in TC, maintaining moderate μ_{nf}[5,6]. The long-term stability of NF remains a major concern, as sedimentation, agglomeration, and particle interactions can degrade their performance over time[7].To address these shortcomings, the HNFs were developed using combinations of two or more types of NPs to achieve synergistic improvements in TC, stability, and rheology[8]. Recent investigations have reported ternary HNFs with three distinct NPs, which sometimes perform better than single- and binary-NF systems in terms of HT efficiency, thermal stability, and flow consistency[9,10].These enhanced properties were the results of geometrical, structural, and interfacial synergies among multiple NPs for the benefit of energy transport with less aggregation in the base fluid. Thus, hybrid and ternary HNFs show remarkable potential for applications, such as heat exchangers, solar collectors, and thermal energy storage systems.

Wanatasanapan et al.[11] studied the effects of changing TiO_2-Al_2O_3 NPs mixing ratios on the TC, rheological behavior, and μ_{nf} values of water (H_2O)-based HNFs, where the examination involved NFs at a 1.0% volume concentration of NFs. An examination of five different NP ratios at a temperature (T) and influent range of 30–70 °C showed that the maximum TC (1.134 W/m·K) was achieved at a 50:50 ratio at 70 °C, with a 71% enhancement compared to using deionized H_2O. In addition, NFs exhibited Newtonian flow, with a maximum μ_{nf} of approximately 1.98 mPa·s at the 80:20 ratio. Mousavi et al.[12] conducted experimental investigations to measure the convective HT and pressure drop performance of SNFs, BHNFs, and THNFs in a horizontal pipe, with fully developed turbulent flow. The enhancements for HT rates and pressure drop were further remarkable, particularly using THNFs at 60:30:10 Volume Fractions (ϕ). The maximums included in THNFs showed an increase of 72% for the HT coefficient and a reduction of 48% for pressure. Sundaram et al.[13] studied and applied a SiO_2-NPs hybrid vehicle cooling system to analyze its thermal properties. They prepared an NF from SiO2 NPs at 0.1–0.5% concentration in a 50:50 mixture of ethylene glycol and H2O (distilled H_2O). They determined that μ_{nf} for NFs increased at TC with concentrations higher than 0.5%. They reported a 20% increase in TC relative to pure ethylene glycol at 120 °C. The studies indicated that SiO2-NFs had the potential to enhance HT in cooling applications with only slight changes in μ_{nf}. Kanti et al.[14] constructed hybrid NFs consisting of Al2O3 and GO at two different ratios, 50:50 and 80:20, aiming to yield enhanced thermophysical properties and HT performance compared to Al_2O_3-only or GO-NF alone. The results show that HT was significantly improved, as the Al_2O_3/GO 50:50 mixture yielded a 64% increase in the Nusselt number (Nu) at 0.5 vol%. Thus, the HT enhancement continued as the pressure drop increased. To predict the thermal characteristics of these NFs, a multi-layer perceptron artificial neural network was employed, achieving high accuracy with R-squared values of 0.98493 (training), 0.98698 (testing), and 0.9837 (validation). Mousavi et al.[15] investigated the thermal and rheological properties of H2O-based dual hybrid NFs (DHNFs) containing CaCO3/SiO2 at nanoparticle concentrations of 0.1%-0.5% and Ts ranging from 15 °C to 60 °C. The experiment examined and analyzed specific heat capacity, TC, resistivity, μ_{nf}, and D, being crucial properties, against available models in the literature. Results suggest that the maximum TC gain was 21.8%, accompanied by a 1.08% increase in heat capacity and a 22.2% reduction in thermal resistivity. Also, the values of μ_{nf} and D increased by 36.9% and 1.2%, respectively. Martínez-García et al.[16] published a comprehensive review on the use of waste wood ash (WWA) as a sustainable alternative in geopolymer concrete and mortar production. The authors argued that WWA is promising as a material when combined with others, such as fly ash, improving compressive strength while providing environmental sustainability benefits. While WWA mainly served as a filler, moderate amounts could still have a positive effect on mechanical and durability properties. Çelik et al.[17] investigated the effects of ground glass powder and crushed glass particles as replacements for fine and coarse aggregates in concrete with varying proportions of 10%, 20%, 40%, and 50%. Mechanical testing (compressive, tensile, and flexural) results showed that glass powder improved concrete performance due to its pozzolanic activity, resulting in a tensile strength increase of up to 14% with partial replacement of fine aggregates. The strength reduced when larger glass particles replaced coarse aggregates due to increased porosity. Pourpasha et al.[18] investigated the enhancement of thermal and dielectric characteristics of insulation oil (INO) using zinc ferrite ($ZnFe_2O_4$) nanoparticles. The findings indicated that at a concentration of 0.1 wt%, a maximum improvement of 14.15% in HT performance and a 17.3% increase in AC breakdown voltage were observed, and the dispersion showed excellent stability over time. This finding clearly showed that $ZnFe_2O_4$-based NFs could significantly enhance both thermal conductivity and electrical insulation reliability. Zeinali et al.[19] analyzed the thermal and exergy performance of a corrugated plate heat exchanger (PHEX) using H_2O-based ternary HNFs containing hydroxyl- and carboxyl-functionalized multi-wall carbon nanotubes (MWCNTs-OH and MWCNTs-COOH). The results indicate that MWCNTs-OH/H_2O and MWCNTs-COOH/H_2O were effective at enhancing the convective HT coefficients by 35.81% and 42.56%, respectively. In comparison, the pressure drop increased by less than 1% at concentrations below 0.06

wt%. The maximum exergy efficiency improvement of 28% was observed at a 0.06 wt% MWCNTs-COOH/H2O ratio and a flow rate of 4.5 L/min. Zeinali et al.[20] analyzed the thermal performance of graphene-COOH/H_2O and TiO_2/H_2O ternary HNFs in plate heat exchangers (PHEX). The thermophysical properties were measured using an experimental procedure, showing that at 0.05 wt%, graphene-COOH/H_2O exhibited an enhanced thermal conductivity of 29.6% and a 27.8% higher convective HT coefficient compared to pure water. TiO_2/H_2O showed a 15.6% improvement in the convective HT coefficient while the pressure drop increased modestly by 3.8%. Graphene-COOH/H_2O-NFs achieved the highest performance index of 1.247 at a Reynolds number of 134.59, indicating a 24.7% enhancement in overall efficiency. As experimentally demonstrated by Basiri et al.[21], the combined effect of natural and forced convection heat transfer in rectangular plate heat sinks was investigated to optimize the air-side thermal performance for cooling applications. The experimental results showed a marked increase in the average Nusselt number with increasing Reynolds number and decreasing fin spacing ratio, accompanied by a decrease in thermal resistance, indicating enhanced heat transfer efficiency. Two empirical correlations were proposed to predict the average Nusselt number for natural and combined convection, with an average deviation of approximately 7%. Pourpasha et al.[22] used ANN integrated with a genetic algorithm (GA) to model and optimize the convective heat transfer performance of Al_2O_3/H_2O, CuO/H_2O, and Cu/H_2O ternary hybrid nanofluids. The numerical results indicated that an increase in Reynolds number from 729 to 1995 at 1 wt% and 96 °C enhanced the Nusselt number(Nu) by 82% for Al_2O_3/H_2O, while Nu was improved by 38% and 77% for CuO/H_2O and Cu/H_2O ternary HNFs, respectively, under similar conditions. Thermophysical behavior and predictive modeling of Fe_3O_4– H_2O magnetic NFs for advanced HT applications were investigated by Sahin et al.[23]. The NFs with concentrations ranging from 0.1 to 1 wt% were synthesized, and stability was confirmed using zeta potential measurements. Experimental TC and μ_{nf} were evaluated between 20 and 60 °C. Two ANN models were developed to predict these properties and zeta potential with high accuracy, yielding a mean square error of 4.51×10^{-6} and a correlation coefficient (R) of 0.99968. Sahin et al.[24] proposed ANN models with high accuracy for predicting TC and zeta potential for Fe_3O_4/H_2O ternary HNFs. The model was trained on experimental measurements of three NP concentrations. The ANN models were found to have Rs >0.99 and very low MSE, while the percentage mean deviation for TC was 0.03%, compared with the new correlation of 0.05%. Despite the multitude of studies on the thermophysical and rheological behavior of nanofluids, they have mainly focused on either one or two systems and have predicted only a single property, namely TC or μ_{nf}, at a time. Although informative, these studies did not account for the complex, nonlinear coupling among many interrelated physical parameters, which ultimately defined the overall performance of HNFs[25]. In fact, to date, no predictive frameworks have existed that allow for the accurate modeling of the combined variation in rheological and density (D) characteristics of ternary HNFs at different temperatures (Ts) and NP concentrations. Typical empirical and semi-empirical correlations were not valid for capturing the interactions described above, as they were based on simple assumptions and couldn't fully describe the dynamic characteristics of multicomponent NF systems[26,27]. The novelty of the present study lies in integrating the development of an ANN framework to predict shear stress (τ), μ_{nf}, and D of a $CuO/CaCO_3/SiO_2$–H_2O ternary HNFs[28]. Such a framework comprised three two-layer feedforward ANN models, built and operated on refined experimental reference data to capture the hidden patterns driving the coupled thermophysical and rheological behavior of the the system. NPϕ and T were input parameters to these models, which modeled the nonlinear dependencies between variation in composition and heat, thereby strengthening data-driven formulations and coupling experimental observations with theoretical predictions of such phenomena. This research presented the first systematic effort to develop a unified ANN-based framework for the simultaneous prediction of multiple key properties in a ternary HNF, thereby superseding empirical approaches with enhanced predictive accuracy and versatility. Thus, the study aimed to design, train, and validate ANN models that accurately predict τ, μ_nf, and D across various operating conditions. This study was limited to the rheological and physical properties of the $CuO/CaCO_3/SiO_2$-H2O system, while thermal transport characteristics were beyond the scope of the present study. The results of this work were anticipated to develop a strong basis for optimizing the formulation and practical application of next-generation HNFs in advanced HT systems.

Performance indicators

A sensitive comparison between the predictions from an ANN model and the actual values, using the appropriate performance metrics tailored to the task, should be performed to assess the ANN model's performance. These metrics demonstrated how well the model captured the complex processes and relationships inferred from the data, thereby providing insight into the predictive capability of the ANN. Performance metrics implicitly contained the most critical information about the model's overall accuracy and the extent to which it deviated from true observed values. Also, this type of information was valuable in identifying potential inadequacies. A basis was being laid for optionally modifying the structural definition of the model or training conditions to achieve a reliable and useful system for real-life applications.

LM optimization algorithm

An LM optimization algorithm was used to train the ANN efficiently, minimizing the sum of squares of prediction errors by iteratively updating the network's weights and biases. The LM method combined the rapid convergence of the Gauss–Newton approach and the numerical stability of the gradient method by approximating the Hessian using the Jacobian of the error vector. This hybrid formulation thus offered sufficient computational efficiency and accuracy for such nonlinear regression problems, making it useful for training feedforward networks in this study[29].

$$f = \sum_{i=1}^{m} e_i^2 \tag{1}$$

In this formulation, m is the number of training samples used in network training. The LM algorithm approximated the Hessian of the loss function using the Jacobian matrix, which consisted of the first-order partial derivatives of the error terms with respect to all adjustable parameters, including weights and biases. The Jacobian provided a measure of how sensitive the output errors were to parameter changes, providing the gradient information necessary for fast, stable optimization[30].

$$J_{i,j} = \frac{\partial e_i}{\partial w_j} \tag{2}$$

Most specifically, i = 1,…,m represents the training sample numbers, and j = 1,…,p denotes the adjustable parameters of the ANN, which relate to the total weight and bias definitions. It is under these definitions that the loss function gradient vector, which is now calculated with respect to the evolution of the loss with respect to every parameter, can be quantified. This vector provides a directional signal to the optimization algorithm for network parameter updates, ultimately reducing prediction error and improving overall model performance[31].

$$\nabla f = 2J^T \cdot e \tag{3}$$

In equation three, the vector e denotes the residuals between the predicted and target outputs for all training samples. In the LM optimization scheme, the Hessian H, which is computed from the second-order derivatives of the loss function with respect to the network parameters, is not computed exactly because this is computationally costly. An efficient approximation was obtained using the Jacobian matrix J, which captures the first-order sensitivities of the model errors to changes in its parameters. This substitution exploited the quadratic form of the error function summation, thereby providing a reasonable compromise between computational efficiency and convergence accuracy in ANN training[32].

$$H \approx 2J^T \cdot J + \lambda I \tag{4}$$

A damping coefficient λ is added to the Levenberg–Marquardt algorithm so that the approximated Hessian matrix maintains positive definiteness throughout the optimization process. It added stability to the numerical scheme in cases where the Jacobian was ill-conditioned or the solution was far from the minimum. By adaptively tuning λ, the algorithm can combine the Gauss-Newton and gradient-descent update mechanisms to achieve both stable convergence and effective parameter refinement.

$$w^{(i+1)} = w^{(i)} - (J^{(i)T} \cdot J^{(i)} + \lambda^{(i)} I)^{-1} (2J^{(i)T} \cdot e^{(i)}) \tag{5}$$

The MSE

MSE is commonly used as a measure of the performance of regression models. The MSE assesses the accuracy of a regression model by calculating the average of the squared differences between the predicted and actual values. More specifically, MSE was determined by summing the squares of the differences between each observation and its corresponding prediction. Squaring the deviation made it positive, with its positive contribution increasing with greater square error. Thus, larger errors were penalized more heavily. These squared differences were then summed up for every data point and divided by the total number of observations to yield the mean, as given in Eq. 6.

$$MSE = \frac{\sum_{i=1}^{n} (P_{oi} - P_{si})^2}{n} \tag{6}$$

where n is the number of data points, P_{si} and P_{oi} are the ANN output and the actual target corresponding to the i^{th} sample, respectively. Because MSE squares errors, it also amplifies the impact of large errors, making it more susceptible to their effects. A smaller MSE indicates that the model closely matches the actual data, resulting in more accurate and consistent performance.

The correlation (R)

R is a metric used to assess the strength and direction of the linear relationship between predicted outcomes and actual values in a regression model, and is calculated using Eq. 2.

$$R = \frac{\sum_{i=1}^{n} (P_{si} - \overline{P_s})(P_{oi} - \overline{P_o})}{\sqrt{\sum_{i=1}^{n} (P_{si} - \overline{P_s})^2 \sum_{i=1}^{n} (P_{oi} - \overline{P_o})^2}} \tag{7}$$

where, $\overline{P_s}$ and $\overline{P_o}$ are averages of ANN outputs and actual targets corresponding to all data, respectively. R ranges from −1 to 1: a value of 1 indicates a perfect positive relationship, where predicted and actual values increase together; -1 represents a perfect negative relationship, where predicted values increase while actual

values decrease; and 0 suggests no linear relationship. The closer R is to 1 or -1, the more accurately the model predicts; values near 0 indicate weak or no correlation between predictions and actual values.

Train/test methodology

The ANN employed in this study was a feedforward neural network, one of the simplest and most widely used neural network architectures. In a feedforward network, information flows in one direction: from the input layer through the hidden layer (s) (if any) to the output layer[33]. Hence, the information flowed in one direction from the beginning to the output. These networks typically had an input layer, one or more hidden layers, and an output layer. One unique property of feedforward networks was that they did not allow any feedback connections or loops. Whereas recurrent neural networks (RNNs) enable this backward flow of information through the network, they also allow it to pass through the nodes for multiple cycles. The feedforward networks employed backpropagation as a training algorithm. Backpropagation was an iterative training method in which the network's weights were modified and reshaped; it compared the predicted output with the target output, measuring the error. Backpropagation took this error and propagated it backward through the network's weights, causing an update. This loop continued until satisfactory accuracy was achieved. Feedforward networks were also very simple yet flexible, depending on the task they handled, such as classification, regression, or pattern recognition[34,35]. The trial-and-error method was used to determine the architecture of the neural network, including the number of hidden layers and the number of neurons in each layer[36–40]. Several configurations of hidden layers, ranging from 1 to 3, and different numbers of neurons, ranging from 3 to 10, were tested for prediction accuracy, generalization capability, and computational efficiency. The architecture that produced the most stable convergence with the lowest total prediction error while avoiding overfitting was that consisting of two hidden layers with five neurons per layer. For the purpose of developing predictive models for the estimation of τ, μ_{nf}, and D of the aqueous $CuO/CaCO_3/SiO_2$ ternary HNFs, three feedforward ANNs were constructed and trained in MATLAB R2015b. The architecture and training of the networks were managed using the built-in newff command, giving control over network structure, training function, and optimization parameters. Each network was trained using the Levenberg-Marquardt (LM) optimization algorithm with error backpropagation, which iteratively adjusted the weights and biases to minimize the mean squared error (MSE) between the predicted and target values. In this study, the dataset consisted of 30 samples for τ, 60 for μnf, and 60 for D, which were divided into three parts: 60% for training, 20% for validation, and 20% for testing. The input and output data were normalized to the range of 0 to 1 to improve convergence and numerical stability. The activation functions for the hidden and output layers were the tangent sigmoid and linear functions, respectively. The training was automatically stopped if the validation error did not improve for 10 consecutive iterations, thus avoiding overfitting and ensuring reasonable generalization. This methodology ensured numerical stability, computational efficiency, and accurate prediction for thermophysical properties of ternary HNFs. Figure 1 shows the architecture of the backpropagation neural network for τ, μ_{nf}, and D prediction.

K-fold cross-validation

Cross-validation in k-fold was recognized as one of the most accepted and effective techniques for validating the precision and generalization capability of machine learning models. The k-fold cross-validation technique involves partitioning the dataset into k equal, non-overlapping subsets, known as folds. In each iteration, the model was trained on $(k-1)$ folds and tested on the remaining fold, ensuring that each fold served as a validation set. Ultimately, the average across all folds yielded an overall model performance estimate that was an excellent predictor of predictive accuracy and helped prevent overfitting. This study randomly divided the data into 10 mutually exclusive subsets of approximately equal size and performed 10-fold cross-validation to validate the ANN model. The result, as illustrated in Fig. 2, shows that the average RMSE for predicting τ was 0.0008 Pa, which was indeed very small compared to the experimental range of 0.0140 to 0.1212 Pa. This low error indicated that the neural network was indeed capturing the nonlinear relationship between the input

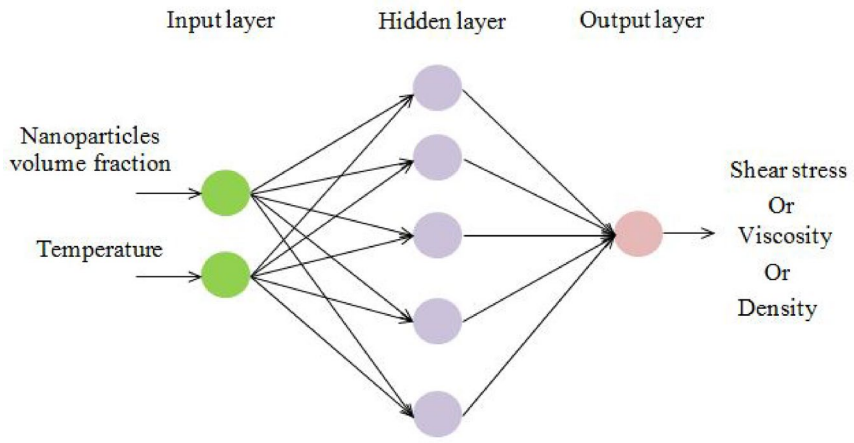

Fig. 1. Architecture of the backpropagation neural network for τ, $\mu_{nf,}$ and D prediction.

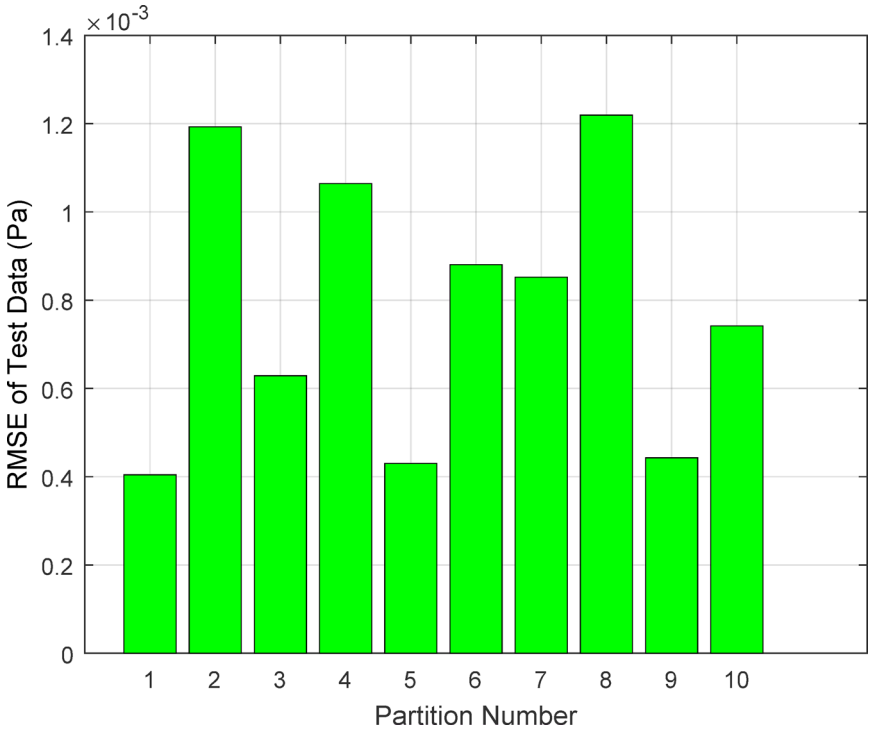

Fig. 2. RMSE of τ test data corresponding to 10 partitions created by the K-fold cross validation approach.

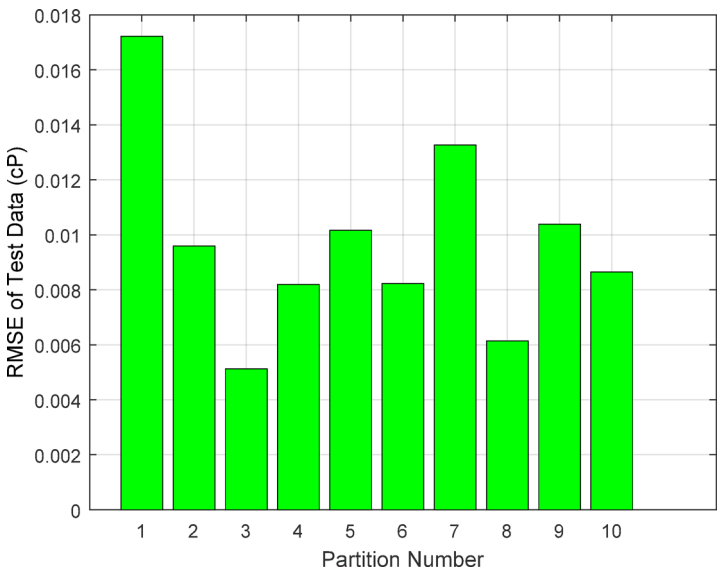

Fig. 3. RMSE of μ_{nf} test data corresponding to 10 partitions created by the K-fold cross validation approach.

parameters and the target variable τ. RMSE values across the 10 folds were consistent, indicating that the model generated stable and reproducible results and demonstrating its potential to generalize effectively to unseen data. This consistent performance showed that the ANN architecture, learning rate, and number of neurons were well-defined for this application, thereby enabling the network to achieve a good balance between bias and variance. The poor spread of fold errors also indicated that the training and validation datasets must be well-distributed so that the predictive model is not trained on any particular section of the data.

Figure 3 presents the RMSE values obtained from the tenfold cross-validation procedure used to predict the μnf of ternary HNFs. The overall RMSE of the tenfold analysis was 0.0097 cP, which was small when contrasted to the experimental μ_{nf} range of 0.4659 to 1.5698 cP. Such a tiny error indeed stated that ANN fit very well to the nonlinear correlation structure of μ_{nf}, T, and NPs–ϕ. The consistency of the RMSE across the ten folds confirmed the model's stability during training and validation. The similar magnitude of RMSE across all folds

demonstrated that the model was neither over-trained nor under-trained, indicating a strong generalizing ability. This suggested that the network, while predicting μ_{nf} values for unseen data, maintained an acceptable level of bias-variance trade-off. Also, the low dispersion in RMSE ensured that the training dataset was fairly representative of the physical behavior of the HNFs so that the ANN was able to identify the complex interplay among the changes in particle loading and T. Furthermore, this indicated that the ANN model developed captured the thermoviscous response of $CuO/CaCO_3/SiO_2$-H_2O-NFs under varying experimental conditions well. Those mentioned above were consistent with network predictions, demonstrating the robustness of this approach as a data-driven modeling framework for μNF behavior in HNFs, which are often characterized by time and cost constraints in experimentation.

In Fig. 4, the RMSE values obtained from 10-fold cross-validation predict D of the $CuO/CaCO_3/SiO_2$-H_2O ternary HNFs. The mean RMSE across the 10-fold procedure was 0.0003 g/cm³, which was negligible as compared to the experimental D range of 0.9832–1.0194 g/cm³. The low error confirmed that the ANN had high accuracy and could effectively simulate the nonlinear variation of D to T and NPs–ϕ. The uniformity of RMSE values across the ten folds suggested that the ANN learned with a consistent behavior during training and showed neither overfitting nor underfitting. This consistency further implied an optimal choice of network architecture and all training parameters for this task. Less sensitive to minor increments in NP concentration than μ_{nf} or τ, the small RMSE variation was another validation of the ANN's ability to recognize subtle changes due to both thermal expansion and particle loading effects. On the whole, its stability across folds indicated it can transfer the knowledge to any new dataset while preserving physical correctness. The small predictive errors underscored that the ANN not only fit the experimental data well but also remained numerically robust across a wide range of variations in thermal and compositional conditions.

Prediction results and analysis

Comparison of different performance functions

The performance curve of the ANN for estimating τ is shown in Fig. 5, which shows a trend in MSE across the training, validation, and testing phases. The graph shows that MSE values continued to decrease during the learning process, indicating network optimization and improved prediction accuracy. There was a decreasing trend in error, indicating that the ANN successfully captured the nonlinear relationship between the input parameters and τ by adjusting its weights to minimize prediction errors. The green marker on the curve indicates the iteration at which the best validation performance occurred: the 239th, with an MSE of 6.2197×10^{-6}; thus, this point represents the best trade-off between minimizing training error and maintaining generalization on unseen data. The difference between the training and validation errors was also quite small at this iteration, indicating that the model could avoid overfitting, which was necessary for robust prediction. In addition, the overall MSE across the entire database, including training, validation, and testing, was the lowest at 1.6321×10^{-6},

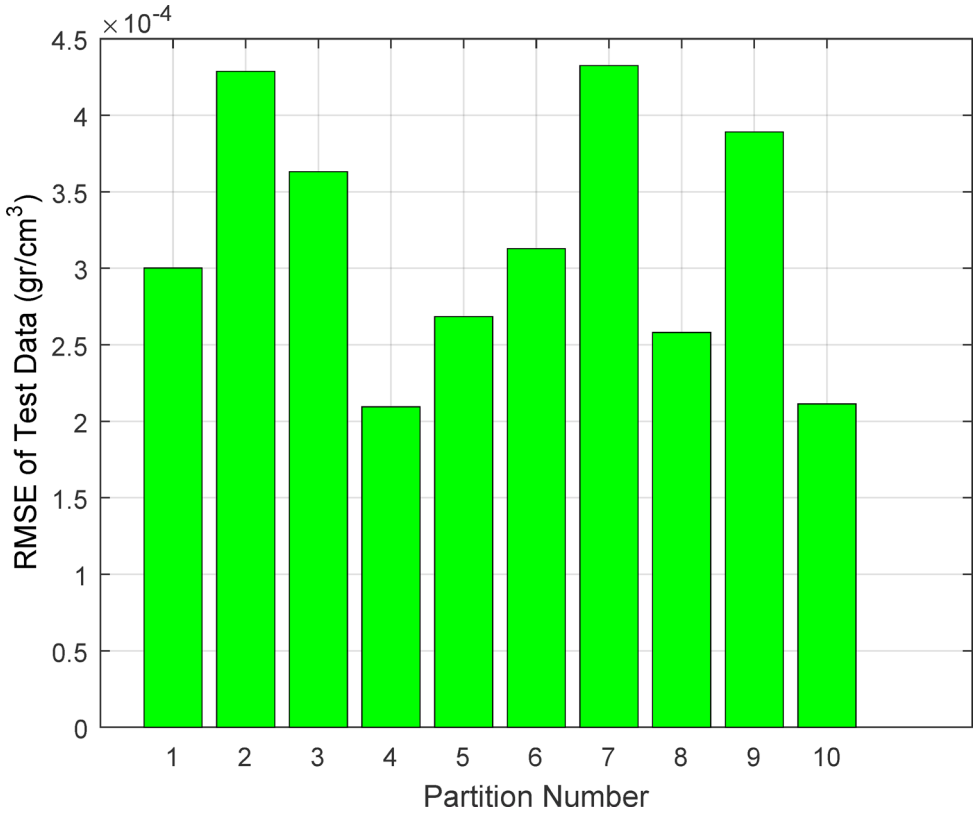

Fig. 4. RMSE of D test data corresponding to 10 partitions created by the K-fold cross validation approach.

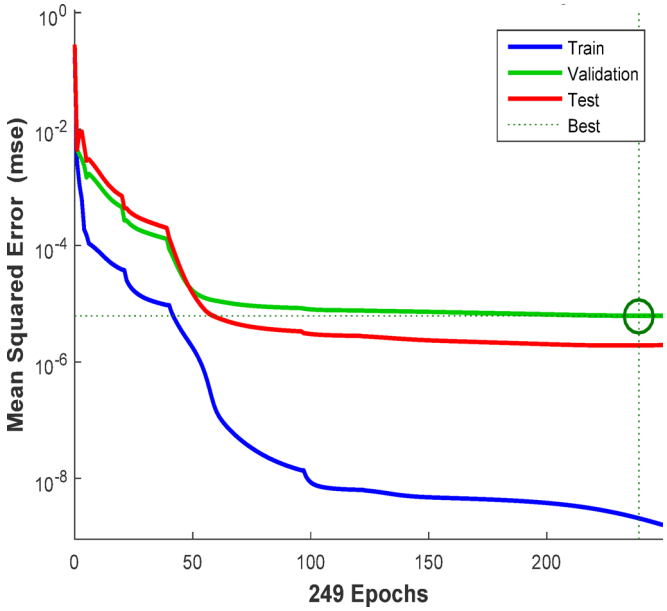

Fig. 5. ANN performance graph during the optimization stages of the corresponding MSE index for each set of training, validation, and NFs-τ test data.

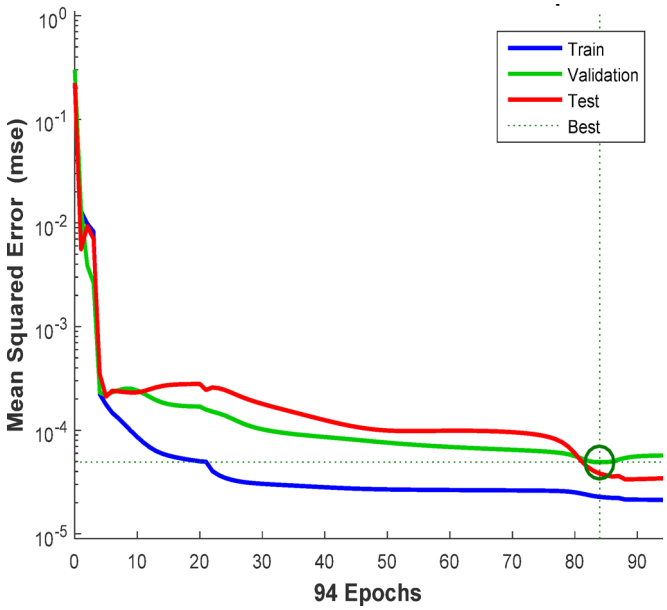

Fig. 6. ANN performance graph during the optimization stages of the corresponding MSE index for each set of training, validation, and NFs- μ_{nf} test data.

indicating very good accuracy and numerical stability achieved by the ANN. Such a small error indicated that the selected choices for the network architecture, learning algorithm, and hyperparameters were appropriate, allowing the model to converge effectively while maintaining generalization quality. In all, the performance graph clearly showed that the ANN achieved stable learning, high prediction precision, and reliable convergence, demonstrating it to be an excellent model for analyzing the complex, nonlinear dependencies correlated with τ behavior in HNFs.

Figure 6 shows the ANN performance curve for predicting ternary HNFs μ_{nf}, illustrating the variation in MSE during training, validation, and testing. Apparently, with increased iterations, the MSEs tended to decrease, indicating that, over time, the network's learning progressed and achieved consistent reductions in error. Perhaps it demonstrated that the ANN successfully captured the non-linear dependency of μnf on T and NPs-ϕ, while remaining numerically stable during optimization. The best validation performance was achieved in iteration 84,

with an MSE of 4.92×10^{-5}, as indicated by the green marker in the plot. This was the optimal point at which the network achieved a commendable trade-off between reducing training error and generalizing to unseen data. The small difference between the training and validation curves furthers the argument that the network was well-regularized and not overfit. Not only this, but also the recording of the minimum overall MSE across the datasets, which is folded to give a single value of 3.1120×10^{-5}, indicative of high precision and low reliability by the ANN in predicting μnf conditions. This performance indicated the appropriateness of the selected network structure and training parameters for modeling the complex thermoviscous behavior of HNFs.

In Fig. 7, the network performance curve for the artificial neural networks predicting the diffusion coefficient of ternary $CuO/CaCO_3/SiO_2–H_2O$ hybrid nanofluids was displayed. This graph shows the progression of the MSE during training, validation, and testing. A downward trend was observed throughout the learning process, indicating that the entire ANN learning process progressively optimized predictions and led to a subsequent decrease in estimation error. This implied that the model learned the underlying nonlinear relationship between D, T, and NPs–ϕ. The validation performance peaked at 107 with MSE 2.2613×10^{-5}, as denoted by the green marker in the plot. At this point, the optimization process achieved a perfect fit to the training data while maintaining sufficient generalization capability for unseen fresh samples. The proximity of the training and validation error curves further confirms that there was no evidence of overfitting and that regularization during learning maintained the balance. Furthermore, the combined Min overall MSE across all datasets (training, validation, and testing) was 4.0385×10^{-5}, demonstrating the network's excellent accuracy and numerical stability. These error values confirmed that the model indeed proved its worth in discerning minute changes in D, engendered by T-induced expansion and NP loading effects. Hence, the ANN can be regarded as a robust and efficient predictive system for estimating the D of HNFs, thereby greatly assisting the design and optimization of high-performance thermal and energy systems.

The dependence plot for an ANN developed to predict the τ of $CuO/CaCO_3/SiO_2$-H_2O ternary HNFs is shown in Fig. 8. The data shown in this graph are actual experimental values and predicted outputs for the training, validation, and test datasets, compared with all other datasets. Data points, in perfect agreement in both predicted and actual values, should be aligned along this 45° reference line. The close clustering around this line indicates that the ANN achieved a high degree of accuracy across all datasets for that model. In the prediction model, Rs were 1.0000 for training, 0.99997 for validation, 0.99999 for testing, and 0.99999 for the overall dataset. Nearly identical to the ideal correlation value of 1.0000, these values indicated an extremely strong linear relationship between ANN predictions and target outputs. These high R values confirmed that the network was able to reasonably capture the nonlinear physical relations τ, T, and NPs-ϕ, resulting in a very small deviation from the experimental data. This uniformity in regression performance across all subsets further indicated good training of the ANN, corroborating its effective generalization on new data. Whenever the network showed consistency in alignment with an internal structure and learning parameters, it ensured

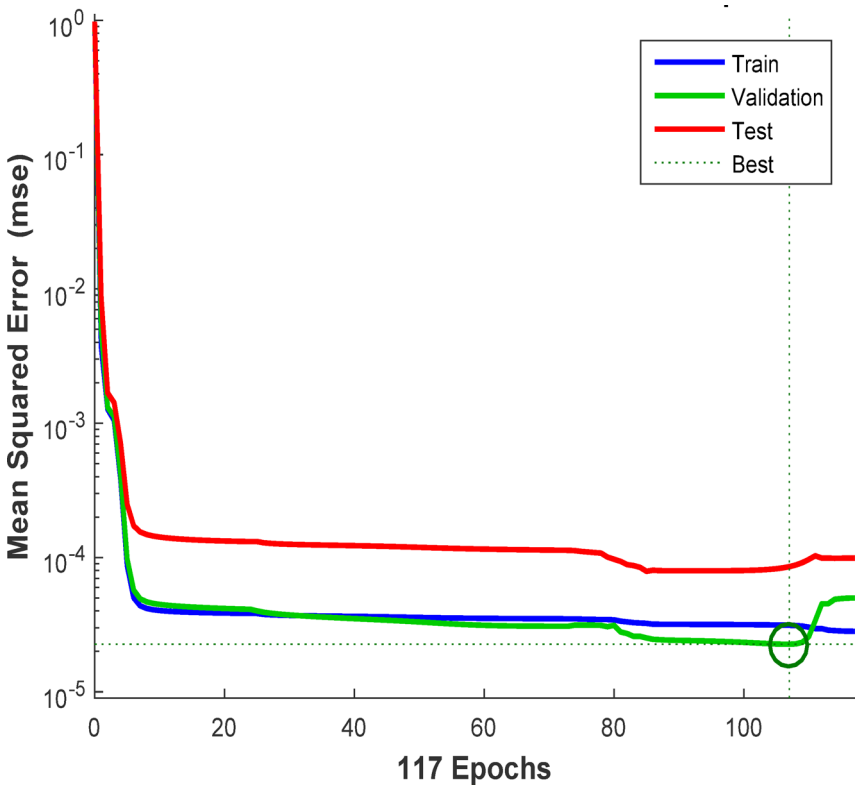

Fig. 7. ANN performance graph during the optimization stages of the corresponding MSE index for each set of training, validation, and NFs-D test data.

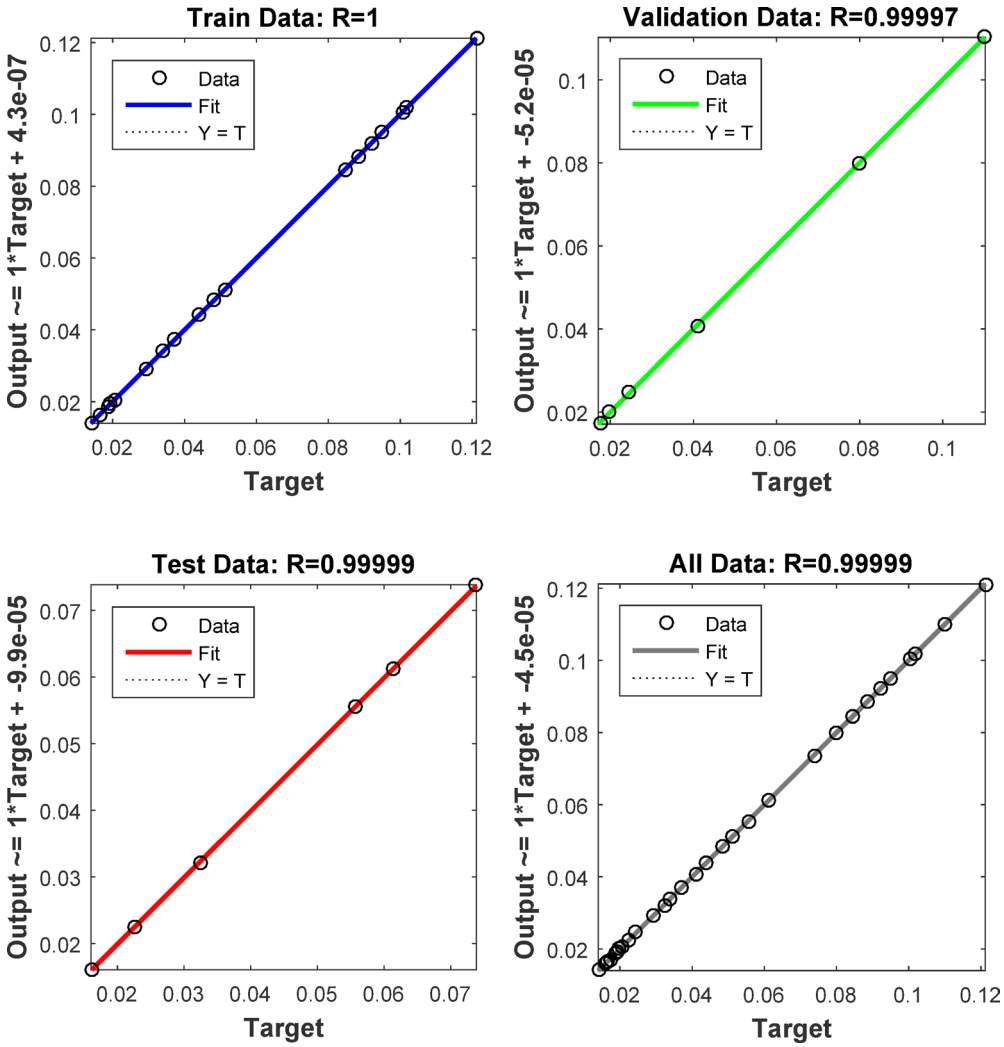

Fig. 8. ANN regression plot corresponding to NFs-τ output for each set of training, validation, and testing data.

numerical stability and predictive accuracy. Thus, the ANN presented a reliable, physically realistic model for estimating τ of HNFs, providing insight into their complex rheological behavior under different thermal and compositional conditions.

This document shows Fig. 9, a regression plot for the ANN used to predict the μ_{nf} of $CuO/CaCO_3/SiO_2$-H_2O ternary HNFs. Predicted μ_{nf} values were compared with each of the corresponding experimental targets for the training, validation, and testing datasets. Close clustering of data points around the surround reference at 45 degrees showed that the ANN actually predicted very close values, lying exactly on this line, with exact agreement between predicted and actual values. The R values for training, validation, testing, and the complete dataset were 0.99983, 0.99952, 0.99963, and 0.99972, respectively, values that are very close to unity, indicating that the network captured the nonlinear relationship among μnf, T, and NPs-φ with very low deviations. The observed slight deviations were small enough to ensure the model maintained very high predictive reliability, avoiding both underfitting and overfitting during training. This close agreement between the predicted and measured μ_{nf} values indicated that the ANN can effectively simulate the thermoviscous behavior of HNFs across different operating conditions.

The regression plot for the ANN designed to predict the D of $CuO/CaCO_3/SiO_2$–H_2O ternary HNFs is shown in Fig. 10. The predicted D values were plotted against the experimental values for the training, validation, and testing sets. The regression coefficients of the D estimation network were 0.99974 for training, 0.99976 for validation, 0.99904 for testing, and 0.99965 for the whole dataset. Such R values, very close to unity, demonstrated a strong linear correlation between ANN predictions and experimental data. Variations, although small, among the three phases—training, validation, and testing—were within acceptable limits, confirming the network's consistency and robustness across varying T and NPs–ϕ conditions. The ANN's regression slope and bias were also close to 1.0 and 0.0, respectively, validating its strong linearity and absence of systematic errors.

Figure 11 shows the comparative fitting of experimental and predicted τ values for the test dataset, along with the corresponding percentage error distributions for the ANN model. Strong overlap between predicted

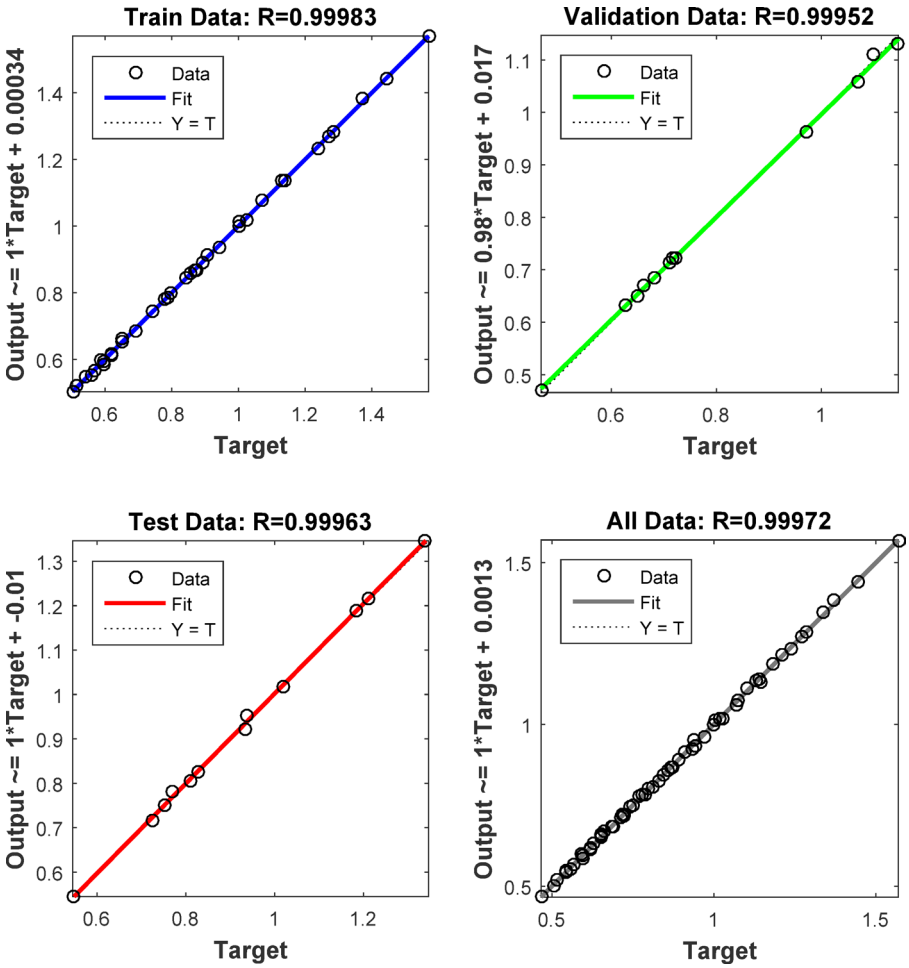

Fig. 9. ANN regression plot corresponding to the NFs- μ_{nf} output for each set of training, validation, and testing data.

and measured τ values indicated that the ANN performed a commendable job of predicting and reproducing the nonlinear dependence of τ on input parameters. This means the model learned the complex interactions governing the rheological behavior of the ternary HNFs. As shown in the lower part of the figure, the relative error was consistently less than 1% across all test samples, providing strong evidence of the accuracy, stability, and reliability of the trained ANN. Additionally, there was no systematic trend or bias in the error distribution, indicating that the model neither underfitted nor overfitted during learning. Overall, this indicated that ANN captured the intrinsic physical correlations among T, NPs-ϕ, and the resulting τ variations with high fidelity.

Figure 12 compares the ANN-predicted and experimental μ_{nf} values for the test dataset, providing a quantitative measure of ANN predictive accuracy. The close overlap between predicted and actual data points confirmed that the ANN reasonably captured the nonlinear, T-dependent behavior of μnf in $CuO/CaCO_3/SiO_2$–H_2O ternary HNFs. This agreement indicated that the network learned the complex interrelations among the input parameters that govern the thermoviscous response of the suspension, such as NPs-ϕ and fluid temperature. The relative distribution of errors further validated this model. The relative errors generally remained within a very small range around the zero-error line, indicating that any deviations between the predicted and experimental values for μ_{nf} were minuscule. The absence of any systematic trend or bias in the test samples showed that the ANN generalized well without being overfit. This uniform spread in prediction errors indicated the network's degree of accuracy in modeling the physical dependence of μnf on thermal and compositional variables.

Figure 13 shows the performance of ANNs constructed to predict the D of $CuO/CaCO_3/SiO_2$-H_2O ternary HNFs. ANN learns the complex, non-linear dependency of D on T and NPs-ϕ very well, while maintaining stable convergence characteristics during training within the required range for making predictions consistent with physical considerations. The distribution of relative error further aided in establishing the model's predictive reliability through simulation. The error values were characteristically low and symmetrically distributed around the zero-error line, indicating that deviations between predicted and experimental values were not considerable. Such absence of grouping or systematic bias in errors indicates a strong generalization capability of the network, as evidenced by the details, which indicate how well the interplay between NPs-ϕ, T, and the resulting D variations emerged. A nearly even distribution of low error magnitudes indicated that the ANN did not overfit and performed equally well on both the training and unseen test sets.

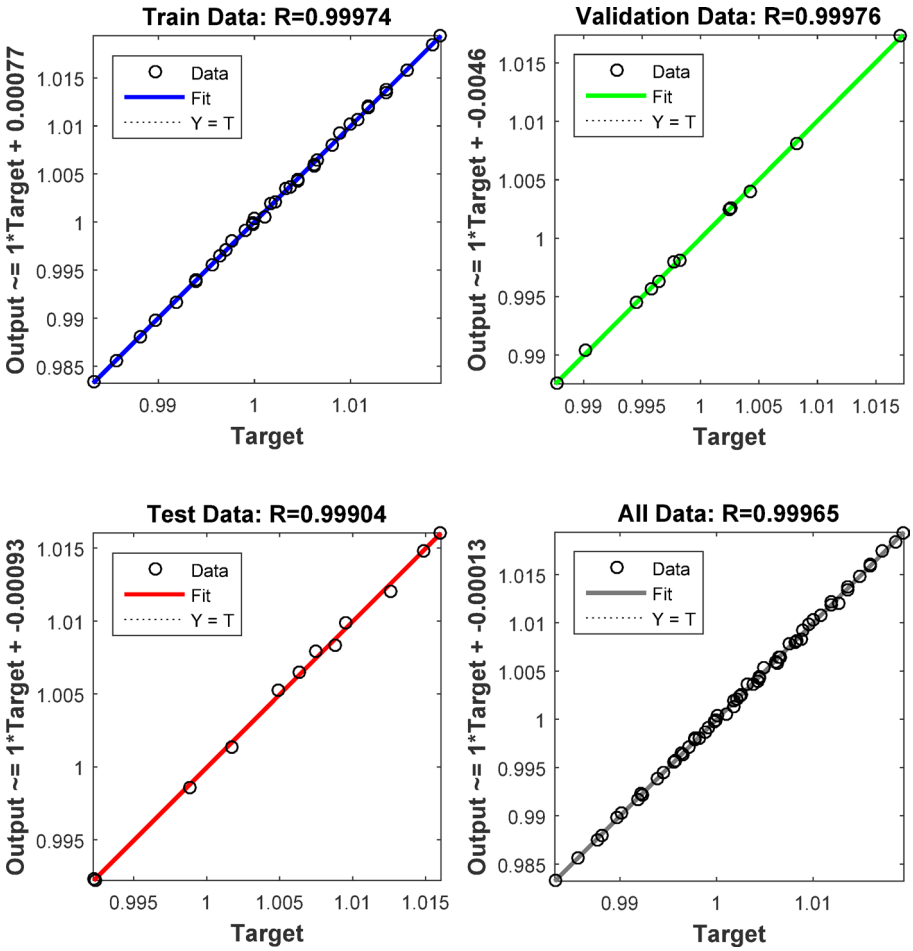

Fig. 10. ANN regression plot corresponding to NFs-D output for each set of training, validation, and testing data.

Shapes of fitted functions

The distribution of relative errors between predicted and experimental τ values for all laboratory data included in this study is illustrated in Fig. 14. The data were compared across a wide range of Ts and NPs-ϕ in the base fluid to evaluate the accuracy and reliability of the developed ANN. The maximum relative error in τ estimation was 0.7059%, while the average relative error was 0.3297%, both of which are very small. These results confirmed that the ANN could predict τ with excellent accuracy across varying thermophysical conditions, further corroborating the model's robustness. The minimum absolute error of 1.3493×10^{-7} Pa indicated that the network ultimately reproduced the target outputs with a very small deviation. The maximum error of 4.6628×10^{-4} Pa and the mean error of 7.3617×10^{5} Pa also indicate that the differences between the predicted and experimental values were very small throughout this dataset. The uniform distribution of relative errors indicated consistent model performance across the entire range of testing conditions, without apparent bias or trends, and strong generalization capabilities. These findings jointly affirmed the predictive reliability and numerical stability of the proposed ANN. Furthermore, the model's ability to maintain predictions with errors below 1% confirmed its capability to accurately model τ behavior in HNFs. Such precision was crucial for investigating the rheological nature of these materials to enhance flow and energy transport performance in advanced thermal systems.

Relative error distribution of μ_{nf} prediction for $CuO/CaCO_3/SiO_2$–H_2O ternary HNFs as a function of T and NPs–ϕ is shown in Fig. 15. This exhaustive analysis was carried out over the entire experimental dataset to assess the quantitative accuracy and generalization performance of the constructed ANN. The highest relative error in μ_{nf} estimation was 1.3417%, while the average relative error was 0.6050%, indicating that the network performed very well in terms of predictive accuracy. These results clearly demonstrate the model's ability to produce experimental μnf values with small deviations, showing its capacity to capture the very complex, nonlinear dependencies of μ_{nf} on thermophysical variables. This further substantiated the reliability and stability of the model. The minimum absolute error was 4.9508×10^{-5} cP, maximum 0.0149 cP, and average 0.0049 cP. The narrow range and near-symmetric distribution of these values around the zero-error axis indicated that the ANN successfully generalized across different thermal and compositional regimes without overfitting or bias. This indicated that the underlying relationships governing μ_{nf} behavior were effectively internalized in the network, including molecular-level interactions between suspended NPs and the base fluid matrix, which governed both viscosity and momentum transfer.

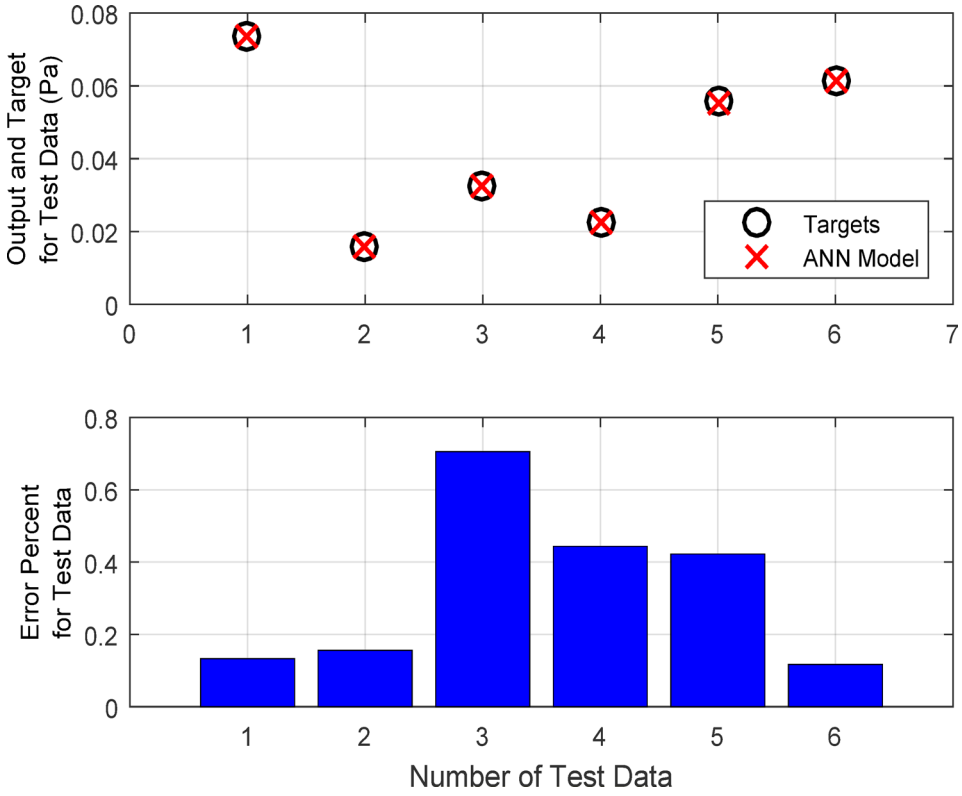

Fig. 11. Matching plots and percentage error between actual τ values and corresponding ANN output, for network test data.

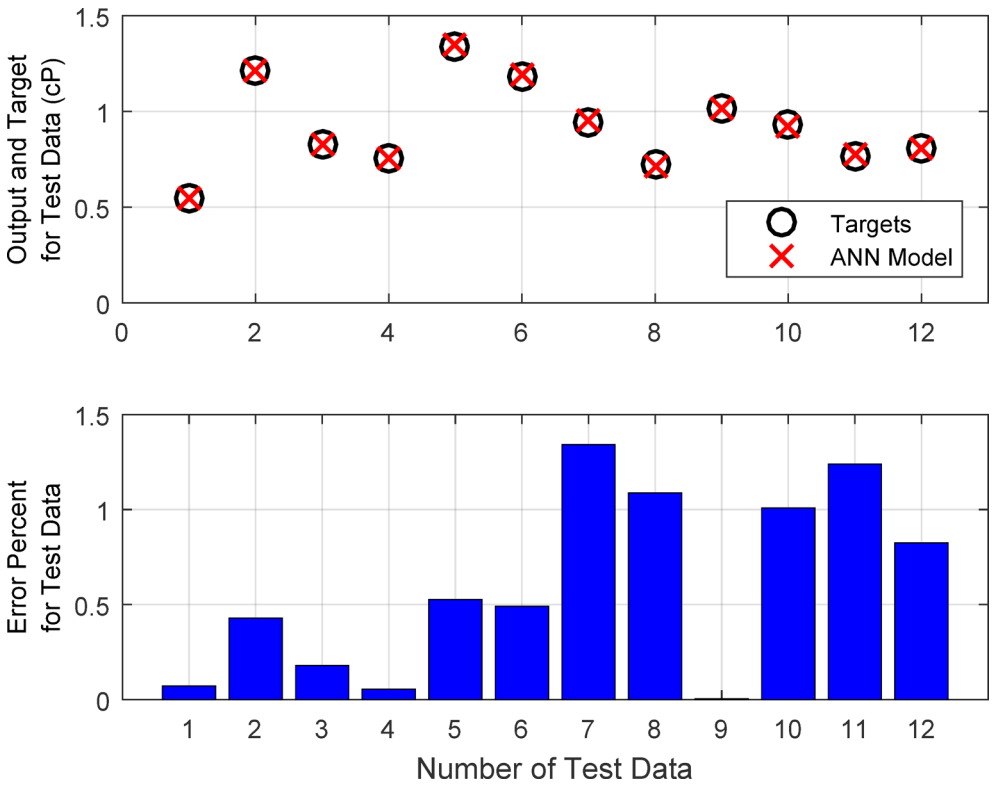

Fig. 12. Matching plots and percentage error between actual μ_{nf} values and corresponding ANN output, for network test data.

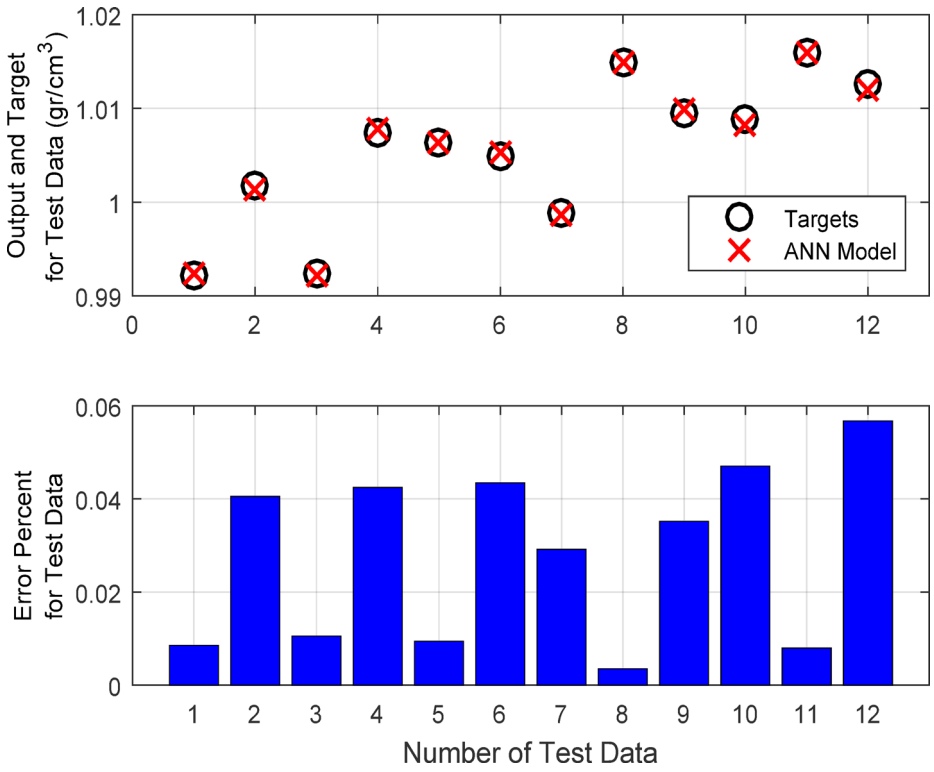

Fig. 13. Matching plots and percentage error between actual D values and corresponding ANN output, for network test data.

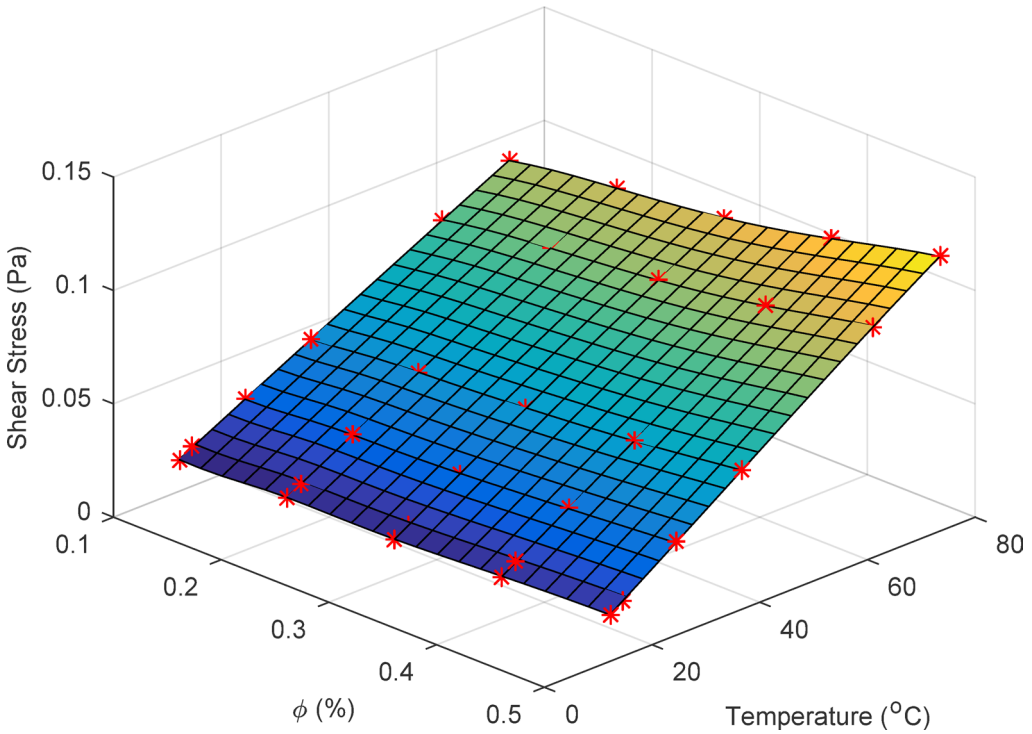

Fig. 14. τ estimation error curve as a function of NFs T and NPs- ϕ in the base fluid for all experimental data.

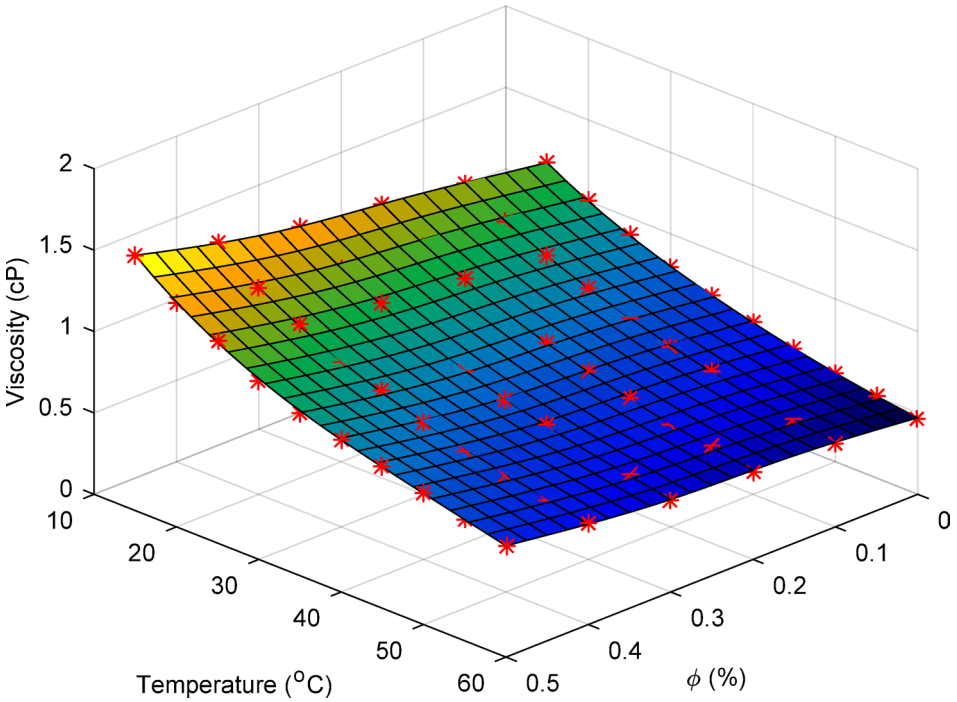

Fig. 15. μ_{nf} estimation error trend as a function of NFs T and NPs- ϕ in the base fluid for all experimental data.

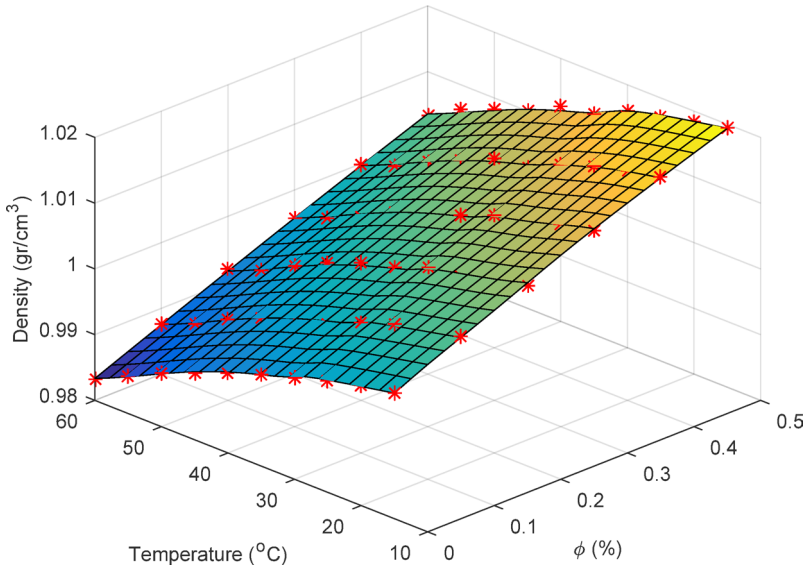

Fig. 16. D estimation error curve as a function of NFs T and NPs- ϕ in the base fluid for all experimental data.

Relative error distribution for D prediction of $CuO/CaCO_3/SiO_2$-H_2O ternary HNFs is shown in Fig. 16. The difference between predicted and actual experimental values is derived from the trained ANN. The maximum and average error percentages were 0.0568% and 0.0279%, respectively. Such low error percentages indicated excellent efficiency and stability of the ANN in reproducing the recorded D data with very high numerical precision, as shown by the detailed error metrics. The minimum absolute error was 1.5137×10^{-6} g/cm³, while the maximum was 5.7473×10^{-4} g/cm³ and the average was 1.7412×10^{-4} g/cm³. The narrow range and small magnitude of values also indicated that ANN displayed excellent prediction consistency across a full range of experimental conditions. Errors were uniformly distributed along the zero-error line, indicating a well-balanced learning mechanism that is free from overfitting and underfitting, and capable of accurate generalization for D, T, and NPs-ϕ. From a physics perspective, a low deviation between predicted and measured values indicates that the ANN was indeed measuring the effects of thermal expansion by NP-induced changes in the fluid's

	Change percentage in NPs- ϕ					Change percentage in NFs T				
ANN Output	2	4	6	8	10	2	4	6	8	10
τ	0.7126	1.4069	2.0915	2.7626	3.4192	1.5973	3.1931	4.7874	6.3799	7.9705
μ_{nf}	1.0533	2.1086	3.1651	4.2221	5.2791	1.1804	2.3294	3.4465	4.5313	5.5832
D	0.0404	0.0801	0.1191	0.1573	0.1948	0.0342	0.0687	0.1033	0.1378	0.1723

Table 1. The maximum change percentage in predicted τ, $\mu_{nf,}$ and D of NFs due to imposing 2- to 10-percent changes on each of the ANN inputs for test data.

	Change percentage in NPs- ϕ					Change percentage in NFs T				
ANN Output	2	4	6	8	10	2	4	6	8	10
τ	0.3664	0.7226	1.0675	1.3998	1.7185	0.9328	1.8653	2.7976	3.7295	4.6611
μ_{nf}	0.4180	0.8448	1.2800	1.7234	2.1747	0.6720	1.3343	1.9871	2.6305	3.2647
D	0.0208	0.0414	0.0620	0.0825	0.1030	0.0122	0.0246	0.0372	0.0499	0.0628

Table 2. The average change percentage in predicted τ, $\mu_{nf,}$ and D of NFs due to imposing 2- to 10-percent changes on each of the ANN inputs for test data.

microstructure, both of which directly affect D. This demonstrated the adequacy of the proposed ANN framework in describing the coupled thermophysical mechanisms underlying HNFs' behavior.

Sensitivity analysis

A detailed sensitivity analysis was conducted to assess the robustness and responsiveness of the developed ANN models. This sensitivity analysis examined the effects of the input parameters NPs-ø and NF-T on the output's τ, μ_{nf}, and D. Besides evaluating the extent to which each model would respond to minor perturbations in input data, the analysis was intended to check how stable the network would be under situations that mimic experimental uncertainties and measurement noise. In this process, each input parameter was perturbed by increments of 2% to 10%, while all other variables were held constant to isolate the specific influence of these parameters. Controlled noise was added to the experimental dataset to simulate realistic deviations and test the model's generalization capacity under rigorous experimental conditions. This analysis yielded critical insights into the reliability and stability of ANN predictions under operational or measurement conditions. As shown in Table 1, as the perturbation magnitude increased, τ, μ_{nf}, and D exhibited maximum deviations proportional to the perturbation magnitude, confirming that the ANN's predictive outputs respond to organized alterations in the input. The influence on τ and μ_{nf} was the greatest, indicating the dominant effect of thermal effects on the rheological and viscous behavior of the NF. The most sensitive to the D predictions are NPs-ϕ changes, as D was directly correlated with particle loading and dispersion stability in the base fluid. These findings provided strong evidence of the physical meaningfulness and high reliability of ANN modeling. These networks were influenced by the input perturbations as expected; however, their prediction scales were within limits and were validated by the robustness and reliability of these models for practical use in property estimates of thermophysical properties for HNFs, which depend on T and concentration.

Table 2 presents the mean percentage changes in the predicted values of τ, μ_{nf}, and D resulting from a 2–10% change in the ANN input parameters for the test dataset. The results were consistent, as greater perturbations in the input data produced larger mean deviations in the predicted outputs. This pattern demonstrated that the ANN models responded regularly to variations in T and NPs-ϕ, confirming the network's physical sensitivity to these influencing parameters. T fluctuations produced higher mean deviations in the values predicted for τ and μ_{nf} compared with those caused by changes in NPs-ϕ. This observation revealed the strong thermal dependence of τ and μnf, typical of HNFs, both of which are significantly affected by T due to the microstructure and interaction forces that the fluid and particles develop. Conversely, the D model showed fairly low overall sensitivity, and the mean variation induced by NPs–ϕ was only marginally above that affected by T. This indicated that D predictions were largely a function of variation in particle loading rather than T, thus consistent with the intrinsic physical nature of D as a mass-dependent property. Overall, the guilt theory demonstrated that when subjected to moderate perturbations in the input variables, ANN models maintained consistent predictive performance. The τ and μ_{nf} networks were more reactive to changes in T. At the same time, the D model was less sensitive, indicating the stability and dependability of the model in addressing the combined effects of thermal and compositional changes within HNFs.

Conclusion

Advancements in engineering applications of HNFs in HT and energy systems require the development of models capable of predicting the complex, nonlinear interactions governing HNFs. In this study, a two-layer feedforward ANN model was developed to predict the three most important thermophysical properties: τ, μ_{nf}, and D for an aqueous $CuO/CaCO_3/SiO_2$ ternary HNFs. The NF system consisted of CuO, $CaCO_3$, and SiO_2 Nanoparticles in volume ratios of 60%, 30%, and 10%, respectively. The model was trained and validated over an extensive range of NPs–ϕ and Ts for generalization and predictive stability. The overall obtained RMSE

results were $\tau = 0.0008$ Pa, $\mu_{nf} = 0.0097$ cP, and $D = 0.0003$ g/cm^3, which were all lower than the experimental ranges by a significant margin, confirming that the ANN could effectively capture the nonlinear correlations between T, NPs–ϕ, and the target properties, exhibiting the model's robustness and ability to generalize well over different thermal and compositional conditions. Highly stable convergence behavior was observed during the optimization of the model using the ANN. The optimal validation MSE of 6.2197×10^{-6} for τ prediction was reached at the 239th iteration, while the best validation MSE for μ_{nf} and D was 4.92×10^{-5} and 2.2613×10^{-5} at the 84th and 107th iterations, respectively. The minimum overall MSEs across all three properties ranged from 10^{-5} to 10^{-6}, indicating the ANN's ability to minimize prediction errors and avoid overfitting. The high numerical stability clearly demonstrated the model's ability to accurately, consistently, and with low deviations predict new data outside the training domain. Meanwhile, R analysis further confirmed the so-called predictive dependence of the ANN, as the R^2 for τ prediction reached unity and remained above 0.9999 in both validation and testing. Likewise, μ_{nf} and D had their R values consistently above 0.9995 and 0.9996, respectively, indicating a strong relationship between the predicted and experimental data. These strong correlations indicated the ANN's proficiency in reproducing complex thermophysical patterns within the HNFs. They confirmed its ability to represent the nonlinear coupling between T, particle concentration, and material response. On the other hand, the error analysis reinforced the consistency and accuracy of the model. Maximum and average relative errors for τ prediction were 0.7059% and 0.3297%, respectively, having absolute errors from 1.3493×10^{-7} up to 4.6628×10^{-4} Pa. For μ_{nf}, the corresponding maximum and average relative errors were 1.3417% and 0.6050%, whilst the corresponding absolute errors varied from 4.9508×10^{-5} to 0.0149 cP. The value of D showed a maximum relative error of 0.0568%; the average reached 0.0279%, and the absolute errors varied from 1.5137×10^{-6} to 5.7473×10^{-4} g/cm^3. The narrow error margins emphasized ANN's greater accuracy in replicating experimental data and its ability to predict thermophysical properties with both high numerical fidelity and physical consistency. Finally, the sensitivity analysis indicated that an increase of input variation from 2% to 10% caused a corresponding increase in the predicted values of τ, μ_{nf}, and D. The effects of T were the greatest on τ and μ_{nf}, thereby confirming the major role played by T in governing rheological and viscous behavior, whereas NPs–ϕ had more influence on D as it indirectly related to mass D and microstructural compactness of suspension. Notwithstanding these sensitivities, the D model was comparatively more stable, thus reflecting balance.

Data availability

The data that support the findings of this study were available from the corresponding author, upon reasonable request.

Received: 5 September 2025; Accepted: 14 November 2025
Published online: 23 November 2025

References

1. Handbook, A. F. American society of heating, refrigerating and air-conditioning engineers (Inc., Atlanta, GA, USA, 2009).
2. Teng, T. P. & Yu, C. C. Heat dissipation performance of MWCNTs nano-coolant for vehicle. *Exp. Thermal Fluid Sci.* **49**, 22–30 (2013).
3. Esfe, M. H. et al. Natural convection in a trapezoidal enclosure filled with carbon nanotube–EG–water nanofluid. *Int. J. Heat Mass Transf.* **92**, 76–82 (2016).
4. Esfe, M. H., Afrand, M., Karimipour, A., Yan, W. M. & Sina, N. An experimental study on thermal conductivity of MgO nanoparticles suspended in a binary mixture of water and ethylene glycol. *Int. Commun. Heat Mass Transfer*. **67**, 173–175 (2015).
5. Esfe, M. H., Rostamian, H., Afrand, M., Karimipour, A. & Hassani, M. Modeling and Estimation of thermal conductivity of MgO–water/EG (60: 40) by artificial neural network and correlation. *Int. Commun. Heat Mass Transfer*. **68**, 98–103 (2015).
6. Khooshechin, M., Fathi, S., Salimi, F. & Ovaysi, S. The influence of surfactant and ultrasonic processing on improvement of stability and heat transfer coefficient of CuO nanoparticles in the pool boiling. *Int. J. Heat Mass Transf.* **154**, 119783 (2020).
7. Songolzadeh, R. & Moghadasi, J. Stabilizing silica nanoparticles in high saline water by using ionic surfactants for wettability alteration application. *Colloid Polym. Sci.* **295** (1), 145–155 (2017).
8. Pugalenthi, S., Devaraj, J., Kadarkaraithangam, J. & Dharmaraj, J. J. J. Improvement in the thermal conductivity and stability of rare-earth metal oxide nanofluids using the stabilizing action of nano CaCO3 in comparison with the stabilizing action of sodium Dodecyl sulphate. *J. Mol. Liq.* **370**, 121056 (2023).
9. Adun, H., Kavaz, D. & Dagbasi, M. Review of ternary hybrid nanofluid: Synthesis, stability, thermophysical properties, heat transfer applications, and environmental effects. *J. Clean. Prod.* **328**, 129525 (2021).
10. Mohammed Zayan, J. et al. Investigation on rheological properties of water-based novel ternary hybrid nanofluids using experimental and taguchi method. *Materials* **15**(1), 28 (2021).
11. Wanatasanapan, V. V., Abdullah, M. & Gunnasegaran, P. Effect of TiO2-Al2O3 nanoparticle mixing ratio on the thermal conductivity, rheological properties, and dynamic viscosity of water-based hybrid nanofluid. *J. Mater. Res. Technol.* **9**(6), 13781–13792 (2020).
12. Mousavi, M., Darvishi, P. & Pouranfard, A. Comparative study of heat transfer and pressure drop in turbulent flow of a singular and hybrid nanofluids into a horizontal pipe. *J. Therm. Anal. Calorim.* **148**(24), 14375–14384 (2023).
13. Sundaram, V., Madhu, S., Vidhyalakshmi, S., Saravanan, A. & Manikandan, S. Characterization of silicon dioxide nanofluids: viscosity and thermal conductivity analysis for hybrid vehicle applications. *SAE Tech. Paper* 0148–7191, (2024).
14. Kanti, P. K., Wanatasanappan, V. V., Sharma, P., Said, N. M. & Sharma, K. Experimental and machine learning insights on heat transfer and friction factor analysis of novel hybrid nanofluids subjected to constant heat flux at various mixture ratios. *Int. J. Therm. Sci.* **209**, 109548 (2025).
15. Mousavi, S. M., Darvishi, P. & Pouranfard, A. Comprehensive study of stability and thermo-physical properties of water-based CaCO3/SiO2 dual hybrid nanofluid. *J. Therm. Anal. Calorim.* **149**(9), 3937–3950 (2024).
16. Martínez-García, R. et al. The present state of the use of waste wood ash as an eco-efficient construction material: A review. *Materials* 15(15), 5349 (2022).
17. Çelik, A. İ. et al. Mechanical behavior of crushed waste glass as replacement of aggregates. *Materials* **15**(22), 8093 (2022).
18. Pourpasha, H., Zeinali Heris, S., Javadpour, R., Mohammadpourfard, M. & Li, Y. Experimental investigation of zinc ferrite/insulation oil nanofluid natural convection heat transfer, AC dielectric breakdown voltage, and thermophysical properties. *Sci. Rep.* **14**(1), 20721 (2024).

19. Heris, S. Z., Pourpasha, H., Abbasi, I. & Ataei, F. Experimental study of exergy-energy performance of stabilized carboxyl-hydroxyl MWCNT/water nanofluids as operating fluid of plate heat exchanger. *J. Ind. Eng. Chem.* (2025).
20. Heris, S. Z. et al. Experimental analysis of graphene-COOH/water and TiO2/Water nanofluids in plate heat exchangers: heat transfer performance and stability. *Renew. Energy*. **245**, 122822 (2025).
21. Basırı, M., Goshayeshı, H. R., Chaer, I., Pourpasha, H. & Herıs, S. Z. Experimental study on heat transfer from rectangular fins in combined convection. *J. Therm. Eng.* **9**(6), 1632–1642 (2023).
22. Pourpasha, H., Farshad, P. & Heris, S. Z. Modeling and optimization the effective parameters of nanofluid heat transfer performance using artificial neural network and genetic algorithm method. *Energy Rep.* **7**, 8447–8464 (2021).
23. Sahin, F., Genc, O., Gökcek, M. & Çolak, A. B. From experimental data to predictions: artificial intelligence supported new mathematical approaches for estimating thermal conductivity, viscosity and zeta potential in Fe3O4-water magnetic nanofluids. *Powder Technol.* **430**, 118974 (2023).
24. Sahin, F., Genc, O., Gökcek, M. & Çolak, A. B. An experimental and new study on thermal conductivity and zeta potential of Fe3O4/water nanofluid: machine learning modeling and proposing a new correlation. *Powder Technol.* **420**, 118388 (2023).
25. Paul, A., Prasad, A. & Kumar, A. Review on artificial neural network and its application in the field of engineering. *J. Mech. Eng. Prakash.* **1**, 53–61 (2022).
26. Baghoolizadeh, M. et al. Multi-objective optimization of annual electricity consumption and annual electricity production of a residential Building using photovoltaic shadings. *Int. J. Energy Res.* **46**(15), 21172–21216 (2022).
27. Rostamzadeh-Renani, M., Baghoolizadeh, M., Rostamzadeh-Renani, R., Toghraie, D. & Ahmadi, B. The effect of canard's optimum geometric design on wake control behind the car using artificial neural network and genetic algorithm. *ISA Trans.* **131**, 427–443 (2022).
28. Mousavi, M., Pouranfard, A. & Darvishi, P. Experimental study and modeling of thermal and rheological characteristics of water-based CuO/CaCO3/SiO2 ternary hybrid nanofluid. *Colloids Surf., A.* **686**, 133367 (2024).
29. Moré, J. J. The Levenberg-Marquardt algorithm: implementation and theory, in *Numerical analysis: proceedings of the biennial Conference held at Dundee, June 28–July 1, 1977* 105–116 (Springer, 2006).
30. Ranganathan, A. The levenberg-marquardt algorithm. *Tutoral LM Algorithm*. **11**(1), 101–110 (2004).
31. Yu, H. & Wilamowski, B. M. Levenberg–marquardt training, in *Intelligent systems*. 12-16 (CRC Press, 2018).
32. Lourakis, M. I. A brief description of the Levenberg-Marquardt algorithm implemented by Levmar. *Foundation Res. Technol.* **4**(1), 1–6 (2005).
33. Zell, A. Simulation neuronaler netze, in Simulation Neuronaler Netze (Oldenbourg Wissenschafts, 1994).
34. Luger, G. F. *Artificial Intelligence: Structures and Strategies for Complex Problem Solving, 5/e*. Pearson Education India (1998).
35. Rashidi, M., Bég, O. A., Parsa, A. B. & Nazari, F. Analysis and optimization of a transcritical power cycle with regenerator using artificial neural networks and genetic algorithms. *Proc. Inst. Mech. Eng., Part A: J. Power Energy* **225**(6), 701–717 (2011).
36. Shang, Y., Hammoodi, K. A., Alizadeh, A., Sharma, K., Jasim, D. J., Rajab, H., … Salahshour, S. Artificial neural network hyperparameters optimization for predicting the thermal conductivity of MXene/graphene nanofluids. *J. Taiwan Inst. Chem. Eng.* **164**, 105673 (2024). https://doi.org/10.1016/j.jtice.2024.105673
37. Basem, A., Abdulaali, H. K., Alizadeh, A., Singh, P. K., Parashar, K., Anqi, A. E., … Maleki, H. Integrating artificial Intelligence-Based metaheuristic optimization with Machine learning to enhance Nanomaterial-Containing latent heat thermal energy storage systems. *Energy Convers. Manage.:X* **25**, 100835 (2025). https://doi.org/10.1016/j.ecmx.2024.100835
38. Hasan, N., Aljibori, H. S. S., Hakami, O., Alamri, A. A., Tasneem, S., Khan, M. E., … Safaei, M. R. Ethylene glycol-based nanofluids: machine learning predictions for improved solar thermal performance. *J. Therm. Anal. Calorim.* **150**(12), 9019–9037 (2025). https://doi.org/10.1007/s10973-025-14271-z
39. Wang, Z., Shami, H. O., Kazim, K. J., Basem, A., Al-fanhrawi, H. J., Dacto, K. E. C., … Ali Eftekhari, S. Using different Heuristic strategies and an adaptive Neuro-Fuzzy inference system for multi-objective optimization of Hybrid Nanofluid to provide an efficient thermal behavior. *Swarm Evol. Comput.* **86**, 101536 (2024). https://doi.org/10.1016/j.swevo.2024.101536
40. Hai, T., Basem, A., Alizadeh, A., Singh, P. K., Rajab, H., Maatki, C., … Maleki, H. Optimizing ternary hybrid nanofluids using neural networks, gene expression programming, and multi-objective particle swarm optimization: a computational intelligence strategy. *Sci. Rep.* **15**(1), 1986 (2025). https://doi.org/10.1038/s41598-025-85236-3

Funding

General Scientific Research Project of the Education Department of Zhejiang Province (Grant No. Y202353333).

Declarations

Competing interests

The authors declare no competing interests.

Additional information

Correspondence and requests for materials should be addressed to A.H.